# Inverse identification of elastic constants using Airy stress function: theory and application

Abdullah A. Alshaya ⬤ · John M. Considine

**Abstract** Development of a novel and efficient inverse method for anisotropic material identification based on a complex-variable formulation of Airy stress function is presented. The overall equilibrium and compatibility, as well as the free traction along the boundary of the internal geometric cutouts, are analytically satisfied by means of conformal mapping and analytic continuation. The inverse problem is posed as an optimization problem where the objective functional is the difference between the measured data and its counterpart evaluated using the complex-variable method. Validity of the proposed inverse method is demonstrated by identifying the elastic constants of a loaded perforated orthotropic member from measured data originated in a region adjacent to a traction-free boundary. Both simulated in-plane displacement components that are superimposed with white noise scatter and experimental strain values were used to illustrate the effectiveness of the proposed method. Numerical experiments indicate that the proposed inverse procedure is capable of accurately characterizing material with large variation of initial estimates of the elastic constants. This alleviates the problem of not knowing a priori the values of the elastic constants. The need to use only few measured data close to the hole boundary and without full-knowledge of the distant geometry and boundary conditions are some advantages of the proposed inverse procedure.

**Keywords** Composites · Inverse problem · Inverse identification · Airy stress function · Complex variables method

A. A. Alshaya (✉)
Mechanical Engineering Department, College of
Engineering and Petroleum, Kuwait University,
P.O. Box 5969, 13060 Safat, Kuwait
e-mail: abdullah.alshaye@ku.edu.kw

J. M. Considine
USDA Forest Service, Forest Products Laboratory,
Madison, WI, USA
e-mail: john.considine@wisc.edu

## 1 Introduction

Stress and failure analyses in engineering practice require a priori knowledge of material mechanical properties. Determining stress concentrations and their locations on the boundaries of geometric discontinuities necessitates accurate knowledge of boundary stresses. Several experimental tests and setups are needed to characterize the elastic constants of the tested material where each of these properties is determined using a specially designed test. These experimental procedures are usually based on applying different loading conditions to a specimen and measuring the applied force and the specimen deformation. Variation of results for these tests requires

several repetitions, and hence several specimens are needed for each loading condition, to have statistically reliable elastic constants. For a complicated material behavior such as anisotropy, characterization becomes more difficult because several different values of the same material property may result from several testing procedures.

Recently, with the aid of kinematic full-field measurement techniques [1] such as digital image correlation (DIC), moiré, electronic speckle pattern interferometry, deflectometry, or grid methods, the tested material can be characterized using inverse approaches, e.g., Finite Element Model - Updating method (FEM-U) [2–6], Constitutive Equation Gap Method (CEGM) [7, 8], Equilibrium Gap Method (EGM), Reciprocity Gap Method (RGM), and the Virtual Fields Method (VFM) [9, 10]. These material identification procedures determine all the elastic constants by performing a limited number of experimental tests. The FEMU, CEGM, and RGM are based on minimizing the difference between the full-field measured data and numerically predicted data, usually from FEM models, using optimization algorithms. EGM and VFM are classified as direct methods for identification of constitutive parameters.

Le Magorou et al. [2] proposed an optimized test to identify the bending/torsion rigidities of composite wood panels from the out-of-plane displacement field. Genovese et al. [3] characterized the in-plane orthotropic material in a composite plate. Molimard et al. [4] identified the mechanical properties of a composite using an open-hole tensile test. Sean et al. [5, 6] measured the interlaminar tensile strength and determined the elastic properties of a uniaxial-compressive perforated composite plate. Gauchait et al. [8] identified the elastic and thermal properties of a heterogeneous material in a two- and three-dimensional domain. Sayed-Muhammed et al. [9] determined the bending stiffness of a thin homogeneous anistropic plate using VFM. Avril and Pierron [11] illustrated the general equivalency of these inverse identification methods. Additionally, Avril et al. [12] provided a general review and comparison between these methods.

Alternatively, the Airy stress function in conjunction with conformal mapping and analytic continuation, usually referred to as complex-variable method (CVM), was recently used to identify material properties from full-field displacement measurements

[13, 14]. The CVM was previously demonstrated as a direct hybrid method for determining the full-field stresses and/or displacements of a loaded composite member with different internal geometric cutouts from different full-field measurements, e.g., thermoelastic stress analysis [15–19], photoelastic stress analysis [20], moiré [21], strain gages [22], or digital image correlation [23]. Advantages of the hybrid CVM over the other hybrid analyses include (1) a smaller experimental data set is required, (2) data can be arbitrarily located, (3) fewer terms in the series representation of the stress function are required to retain, (4) knowledge of the distant loading and boundary conditions is not required, and (5) it is applicable for isotropic and anisotropic homogeneous linear elastic materials.

Prior applications of the hybrid CVM evaluated the full-field stresses and displacements using elastic constants determined experimentally from standard tensile tests. Therefore, a new inverse method for material identification of a loaded perforated composite that is based on minimizing the difference between the measured quantities and the predicted quantities by means of CVM is proposed. The elastic properties are considered as design variables for the optimization scheme. Upon successful identification of the tested material, individual stresses, strains, and displacements can be determined throughout the specimen, including on the edges of holes or cutouts, even with absence of experimental data in those regions.

Unlike VFM which uses the full-field strains for material identification, the proposed technique uses only displacement components and, hence, avoids the challenges associated with differentiation of measured data. Because the technique is based on the strong form of the equilibrium equation, only the interior displacement information is needed in the material identification and without the full knowledge of the distant geometry and boundary conditions. VFM involves the processing of heterogeneous strain fields that requires a well-chosen mechanical test to excite all strain components under known boundary conditions.

Here we propose an inverse identification method of homogeneous anisotropic loaded members based on CVM. To simulate an actual testing and evaluate the reliability of the inverse procedure when using noisy measured displacement data, a numerical experiment is conducted by superimposing white random noise to

the numerically predicted displacement data by means of finite-element analysis. The accuracy of the inverse identification with respect to the number of employed data, the level of the added noise in relation to the variation of results, and the effect of initial estimates to the optimization algorithm are investigated. Finally, the performance of the proposed method was examined using sparse experimental data.

## 2 Complex-variable method

### 2.1 Field equations

The governing equilibrium equations of an elastic solid body with a domain $\Omega$ and a boundary $\partial\Omega$ in a two-dimensional space, Fig. 1, with the absence of body forces and undergoing static deformation can be stated as

$$\frac{\partial \sigma_{xx}}{\partial x} + \frac{\partial \sigma_{xy}}{\partial y} = 0 \qquad \text{and}$$
$$\frac{\partial \sigma_{xy}}{\partial x} + \frac{\partial \sigma_{yy}}{\partial y} = 0 \qquad \text{in} \ \ \Omega \tag{1a}$$

$$\sigma_{xx} n_x + \sigma_{xy} n_y = t_x \qquad \text{and}$$
$$\sigma_{xy} n_x + \sigma_{yy} n_y = t_y \qquad \text{on} \ \ \Gamma_t \tag{1b}$$

where $t_x$ and $t_y$ are the surface traction (external applied forces) with respect to a unit area along the $x$ and $y$ directions, respectively, in the boundary region $\Gamma_t$, and $n_x = \cos(\mathbf{n}, \mathbf{x})$ and $n_y = \cos(\mathbf{n}, \mathbf{y})$ are the outward unit normals to the surface of the body with respect to the global coordinates, $x$- and $y$-axes,
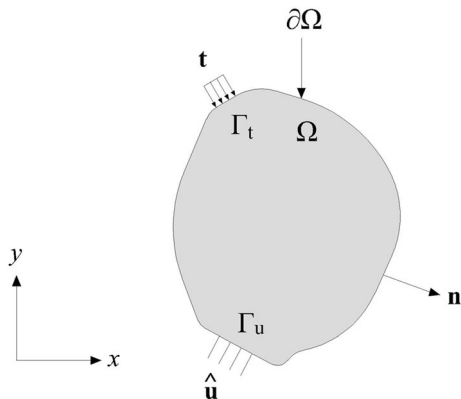


**Fig. 1** Elastic solid body in a two-dimensional space

respectively. The strain–displacement relations are given by

$$\epsilon_{xx} = \frac{\partial u}{\partial x}, \qquad \epsilon_{yy} = \frac{\partial v}{\partial y}$$
$$\text{and} \qquad \epsilon_{xy} = \frac{1}{2}\left(\frac{\partial u}{\partial y} + \frac{\partial v}{\partial x}\right) \quad \text{in} \ \ \Omega \tag{2a}$$

$$u = \hat{u} \qquad \text{and} \qquad v = \hat{v} \qquad \text{on} \ \ \Gamma_u \tag{2b}$$

where $\hat{u}$ and $\hat{v}$ are the prescribed displacements along the $x$ and $y$ directions, respectively, in the boundary region $\Gamma_u$. The boundary regions, $\Gamma_t$ and $\Gamma_u$, that represent the traction (natural) and displacement (essential) boundary conditions are such that $\Gamma_t \cup \Gamma_u = \partial\Omega$ and $\Gamma_t \cap \Gamma_u = \emptyset$. The constitutive equation assuming linear elastic material can be written as

$$\sigma_{\alpha\beta} = C_{ij}\epsilon_{\alpha\beta} \quad \text{where} \ \ \alpha,\beta = x,y \ \ \text{and} \ \ i,j = 1,2,6 \tag{3}$$

where $C_{ij}$ is the second-order linear elastic constitutive tensor. The elasticity tensor can be constant, i.e., homogeneous material, or space-dependent, i.e., heterogeneous material. If the elastic properties are homogeneous orthotropic, these properties can be described in terms of two independent elastic moduli, $E_1$ and $E_2$, a shear modulus, $G_{12}$, and a Poisson's ratio, $v_{12}$.

### 2.2 Airy stress function in complex variable

The equilibrium equation, Eq. (1a), can be satisfied by introducing an Airy stress function, $\mathcal{F}(x,y)$, defined as

$$\sigma_{xx} = \frac{\partial^2 \mathcal{F}}{\partial y^2}, \qquad \sigma_{yy} = \frac{\partial^2 \mathcal{F}}{\partial x^2} \qquad \text{and} \qquad \sigma_{xy} = -\frac{\partial^2 \mathcal{F}}{\partial x \partial y} \tag{4}$$

Differentiating Eq. (2a) gives the compatibility equation,

$$\frac{\partial^2 \epsilon_{xx}}{\partial y^2} + \frac{\partial^2 \epsilon_{yy}}{\partial x^2} = 2\frac{\partial^2 \epsilon_{xy}}{\partial x \partial y} \tag{5}$$

Substituting the strains from Eq. (3) into Eq. (5) and expressing the stress components in terms of $\mathcal{F}(x,y)$ using Eq. (4), one can obtain the equation

$$D_1 D_2 D_3 D_4 \mathcal{F} = 0 \quad \text{where} \quad D_k = \frac{\partial}{\partial y} - \mu_k \frac{\partial}{\partial x} \tag{6}$$
$$\text{and} \quad k = 1, 2, 3, 4$$

The complex material properties, $\mu_k$, are the roots of the following characteristic equation associated with Eq. (6),

$$S_{11}\mu^4 - 2S_{16}\mu^3 + (2S_{12} + S_{66})\mu^2 - 2S_{26}\mu + S_{22} = 0 \tag{7}$$

where $S_{ij} = C_{ij}^{-1}$ for $i, j = 1, 2, 6$ are the material properties (elastic compliances). For a homogeneous orthotropic material $S_{11} = 1/E_x$, $S_{12} = S_{21} = -v_{xy}/E_x$, $S_{16} = S_{61} = 0$, $S_{22} = 1/E_y$, $S_{26} = S_{62} = 0$, and $S_{66} = 1/G_{xy}$, Eq. (7) is reduced to

$$\mu^4 + \left(\frac{E_x}{G_{xy}} - 2v_{xy}\right)\mu^2 + \frac{E_x}{E_y} = 0 \tag{8}$$

Plane problems of elasticity classically involve determining the stress functions, $\mathcal{F}(x, y)$, throughout the elastic solid body $\Omega$ such that the associated stresses and displacements satisfy the boundary conditions, Eqs. (1b) and (2b), around its entire edge $\partial\Omega$. The Airy stress function, $\mathcal{F}$, that satisfies Eq. (6) can be expressed as a summation of two arbitrary analytic functions, $\Phi(z_1)$ and $\Psi(z_2)$, of the two complex variables, $z_1$ and $z_2$, as [24, 25]

$$\mathcal{F} = 2\Re\left[\int \Phi(\mathfrak{z}) \, \mathfrak{d}\mathfrak{z} + \int \Psi(\mathfrak{z}) \, \mathfrak{d}\mathfrak{z}\right] \tag{9}$$

where $\Re$ denotes the 'real part' of a complex number and $z_j = x + \mu_j y$ for $j = 1, 2$.

### 2.2.1 Stresses and strains

The stresses in the rectangular coordinates $(x, y)$ are obtained from Eqs. (4) and (9) as

$$\sigma_{xx} = 2\Re[\mu\Phi'(\mathfrak{z}) + \mu\Psi'(\mathfrak{z})] \tag{10a}$$

$$\sigma_{yy} = 2\Re[\Phi'(\mathfrak{z}) + \Psi'(\mathfrak{z})] \tag{10b}$$

$$\sigma_{xy} = -2\Re[\mu\Phi'(\mathfrak{z}) + \mu\Psi'(\mathfrak{z})] \tag{10c}$$

where primes denote differentiation with respect to the argument. In orthotropic material, the stresses and strains are related by

$$\begin{Bmatrix} \sigma_{xx} \\ \sigma_{yy} \\ \sigma_{xy} \end{Bmatrix} = \frac{1}{1 - v_{xy}v_{yx}} \begin{bmatrix} E_x & v_{xy}E_y & 0 \\ v_{xy}E_y & E_y & 0 \\ 0 & 0 & 2(1 - v_{xy}v_{yx})G_{xy} \end{bmatrix} \begin{Bmatrix} \epsilon_{xx} \\ \epsilon_{yy} \\ \epsilon_{xy} \end{Bmatrix} \tag{11}$$

The displacement are given from Eq. (2a) as

$$u = 2\Re[p_1\Phi(z_1) + p_2\Psi(z_2)] - w_0 y + u_0 \tag{12a}$$

$$v = 2\Re[q_1\Phi(z_1) + q_2\Psi(z_2)] + w_0 x + v_0 \tag{12b}$$

where $w_0$, $u_0$, and $v_0$ are the constants of integration that characterize the rigid body translations ($u_0$ and $v_0$) and rotation ($w_0$), and the other quantities are given as

$$p_j = S_{11}\mu_j^2 + S_{12} - S_{16}\mu_j = \frac{\mu_j^2 - v_{xy}}{E_x}$$
$$q_j = S_{12}\mu_j + \frac{S_{22}}{\mu_j} - S_{26} = -\frac{v_{xy}}{E_x}\mu_j + \frac{1}{E_y\mu_j} \tag{13}$$

where $j = 1, 2$. The rigid body motions, $u_0$, $v_0$, and $w_0$, of a plate loaded in testing machine are zero. The plane problem is now based on determining the two stress functions $\Phi(z_1)$ and $\Psi(z_2)$. A more detailed presentation of this approach is available in references [24, 25] and is included here for sake of completeness.

### 2.2.2 Conformal mapping

A loaded component with a region $\Omega_z$ having a complicated physical $z = x + iy$ shape, $\partial\Omega$, and arbitrarily-shaped traction-free geometric discontinuities, $(\Gamma_0)_h$, is considered in Fig. 2. The plane problem is simplified by mapping each region $(R_z)_h \subseteq \Omega_z$ (for $h = 1, 2, \ldots, r$) containing one of the cutouts into a region $(R_\zeta)_h$ outside a unit circle in the $\zeta = \xi + i\eta$ plane, which has origin at $\zeta = 0$, using the Christoffel–Schwartz mapping function given as

$$z = \omega(\zeta) = R\left(\zeta + \sum_{k=1}^{m} \frac{c_k}{\zeta^{kn-1}}\right) \quad \text{where}$$
$$c_k = \frac{2\Pi_{i=1}^{k-1}(in - 2)}{k!n^k(kn - 1)} \tag{14}$$

where $R$ ($R > 0$) is a constant that defines the size of the cutout and $n$ is the number of sides in the cutout. Many different cutout shapes defined by the individual curves $(\Gamma_0)_h$ in the physical $z$-planes can be mapped
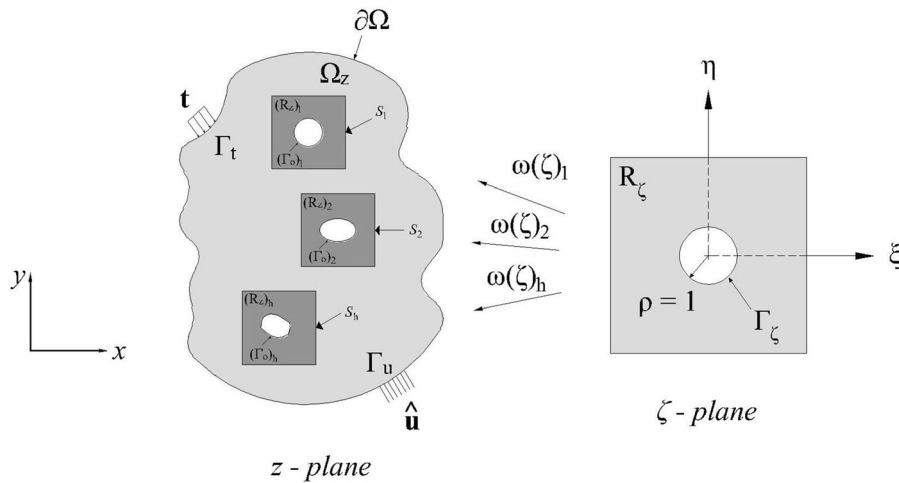
**Fig. 2** Mapping the exterior region of a unit circle in $\zeta$-plane into a general arbitrarily cutout in the physical $z$-plane

into the unit circles $(\Gamma_\zeta)_h$ in the complex $\zeta$-planes by the mapping functions $\omega(\zeta)_h$. The auxiliary planes and their corresponding mapping functions for orthotropic materials are defined in terms of $\zeta_j = \xi + \mu_j \eta$, and hence, $z_j = \omega_j(\zeta_j)$ for $j = 1, 2$.

For instance, the following function maps the region $R_z$ adjacent to a circular cutout of radius $R$ in the physical $z$-plane into the region of the exterior of a unit circle, $R_\zeta$, in the $\zeta$-plane,

$$z_j = \omega_j(\zeta_j) = \frac{R}{2}\left[(1 - i\mu_j)\zeta_j + \frac{1 + i\mu_j}{\zeta_j}\right] \tag{15}$$

for $j = 1, 2$

where the origin of the coordinate system is at the center of the circle. The inverse of the induced mapping functions is

$$\zeta_j = \omega_j^{-1}(z_j) = \frac{z_j \pm \sqrt{z_j^2 - R^2\left(1 + \mu_j^2\right)}}{R(1 - i\mu_j)} \tag{16}$$

for $j = 1, 2$

The branch of the square root in Eq. (16) is chosen such that $|\zeta_j| \geq 1$ for $j = 1, 2$. The induced conformal mapping functions are therefore one-to-one and invertible.

The two analytic stress functions $\Phi(z_1)$ and $\Psi(z_2)$ can therefore be expressed in terms of $\zeta_1$ and $\zeta_2$, respectively, as $\Phi(z_1) = \Phi[\omega_1(\zeta_1)] \equiv \Phi(\zeta_1)$ and $\Psi(z_2) = \Psi[\omega_2(\zeta_2)] \equiv \Psi(\zeta_2)$ and from which the

derivatives with respect to their arguments, $z_1$ and $z_2$, are

$$\Phi'(z_1) = \Phi'(\zeta_1)\frac{d\zeta_1}{dz_1} = \frac{\Phi'(\zeta_1)}{\omega_1'(\zeta_1)} \quad \text{and} \quad \Psi'(z_2) = \frac{\Psi'(\zeta_2)}{\omega_2'(\zeta_2)} \tag{17}$$

The analyticity of the mapping functions ensures that the equilibrium and compatibility are satisfied throughout region $(R_z)_h$ of the physical $z$-plane.

### 2.2.3 Analytic continuation

Consider the subregion $(R_z)_h$ in the physical $z$-plane that has a cutout with a traction-free boundary $(\Gamma_0)_h$, Fig. 2. Using the concept of analytic continuation, the individual stress functions for the mapped region $(R_\zeta)_h$ of the unit circle $\Gamma_\zeta$ in the $\zeta$-plane of an orthotropic material are related to each other by [26, 27]

$$\Psi(\zeta_2) = B\overline{\Phi(1/\overline{\zeta_2})} + C\Phi(\zeta_2) \tag{18}$$

where the constants $B$ and $C$ are defined as

$$B = \frac{\bar{\mu}_2 - \bar{\mu}_1}{\mu_2 - \bar{\mu}_2} \quad \text{and} \quad C = \frac{\bar{\mu}_2 - \mu_1}{\mu_2 - \bar{\mu}_2} \tag{19}$$

The plane problem is now reduced in determining one single stress function, $\Phi(\zeta_1)$. At least for a finite, simply connected region $(R_\zeta)_h$, $\Phi(\zeta_1)$ is a single-valued analytic function. Eq. (18) assumes that the traction-free boundary $(\Gamma_0)_h$ in the $z$-plane can be mapped into the unit circle in the $\zeta$-plane.

### 2.2.4 Mapping collocation

The mapping of the physical $z$-plane into the unit circle in $\zeta$-plane necessitates representing the stress function $\Phi(\zeta_1)$ as the following finite Laurent series

$$
\Phi(\zeta_1) = \sum_{\substack{k=-N \\ k \neq 0}}^{N} A_k \zeta_1^k \tag{20}
$$

where $A_k = a_k + ib_k$ are the unknown complex coefficients ($a_k$ and $b_k$ are both real numbers) and $N$ is any positive integer. The $k = 0$ term in Laurent expansion contributes to rigid-body motion and can be omitted. Substituting Eq. (20) into (18) gives

$$
\Psi(\zeta_2) = \sum_{\substack{k=-N \\ k \neq 0}}^{N} \left( B\bar{A}_k \zeta_2^{-k} + CA_k \zeta_2^k \right) \tag{21}
$$

where $\bar{A}_k$ is the complex conjugate of $A_k$. Substituting Eqs. (20) and (21) into Eq. (10), the individual stresses are

$$
\sigma_{xx} = 2 \sum_{\substack{k=-N \\ k \neq 0}}^{N} \Re \left\{ k \left[ \frac{\mu_1^2}{\omega_1'(\zeta_1)} \zeta_1^{k-1} + \frac{\mu_2^2 C}{\omega_2'(\zeta_2)} \zeta_2^{k-1} \right] A_k - \left[ \frac{k\mu_2^2 B}{\omega_2'(\zeta_2)} \zeta_2^{-k-1} \right] \bar{A}_k \right\} \tag{22a}
$$

$$
\sigma_{yy} = 2 \sum_{\substack{k=-N \\ k \neq 0}}^{N} \Re \left\{ k \left[ \frac{1}{\omega_1'(\zeta_1)} \zeta_1^{k-1} + \frac{C}{\omega_2'(\zeta_2)} \zeta_2^{k-1} \right] A_k - \left[ \frac{kB}{\omega_2'(\zeta_2)} \zeta_2^{-k-1} \right] \bar{A}_k \right\} \tag{22b}
$$

$$
\sigma_{xy} = -2 \sum_{\substack{k=-N \\ k \neq 0}}^{N} \Re \left\{ k \left[ \frac{\mu_1}{\omega_1'(\zeta_1)} \zeta_1^{k-1} + \frac{\mu_2 C}{\omega_2'(\zeta_2)} \zeta_2^{k-1} \right] A_k - \left[ \frac{k\mu_2 B}{\omega_2'(\zeta_2)} \zeta_2^{-k-1} \right] \bar{A}_k \right\} \tag{22c}
$$

The displacements can be obtained from Eq. (12),

$$
u = 2 \sum_{\substack{k=-N \\ k \neq 0}}^{N} \Re \left\{ \left[ p_1 \zeta_1^k + p_2 C\zeta_2^k \right] A_k + p_2 B\zeta_2^{-k} \bar{A}_k \right\} \tag{23a}
$$

$$
v = 2 \sum_{\substack{k=-N \\ k \neq 0}}^{N} \Re \left\{ \left[ q_1 \zeta_1^k + q_2 C\zeta_2^k \right] A_k + q_2 B\zeta_2^{-k} \bar{A}_k \right\} \tag{23b}
$$

The only unknowns in these expressions for the stresses, Eqs. (22), and displacements, Eqs. (23), are the complex coefficients $A_k$ where the other quantities involve geometry (location) and/or material properties.

The concept here is to apply the analysis to any region $(R_z)_h \subseteq \Omega_z$ (as subregions of the overall loaded structure) for $h = 1, 2, \ldots, r$ that has an entire boundary $S_h$ and contains some geometric discontinuity whose traction-free boundary is $(\Gamma_0)_h$. A region $R_h^* \subseteq (R_z)_h$ adjacent to the traction-free edge $(\Gamma_0)_h$ is chosen such that it contains the measured data that have to be employed to determine the complex coefficients, $A_k$. For a significantly large region of interest in a finite structure, additional known boundary conditions may also be imposed at discrete locations. It is worth mentioning that the physical plane $(R_z)_h$ and the traction-free boundary $(\Gamma_0)_h$ can also be mapped into a half-plane, $R_\zeta$, and the real axis of $\zeta$-plane, respectively, where the stress function, $\Phi(\zeta_1)$, in this case is usually represented by a Taylor series.

The induced stresses satisfy equilibrium and traction-free conditions, and the associated strains satisfy compatibility in the adjacent portion of the entire

boundary by means of conformal mapping and analytic continuation techniques. The concept of the *hybrid complex-variable method* in determining the hybrid stresses and displacements of loaded components with different cutouts is based on using measured data in a region $R_h^*$ adjacent to a traction-free edge $(\Gamma_0)_h$, mapping the region $(R_z)_h$ into $(R_\zeta)_h$ such that $(\Gamma_0)_h$ of the physical $z$-plane is mapped into the unit circle in the $\zeta$-plane, relating the two stress functions to each other by means of analytic continuation, and satisfying other boundary conditions discretely beyond the traction-free $(\Gamma_0)_h$.

### 2.3 Determination of the unknown coefficients

The displacements and stresses throughout the subregion $(R_z)_h$ can be written in a matrix notation as

$$\mathbf{u} = \mathbf{U}\mathbf{c}, \qquad \mathbf{v} = \mathbf{V}\mathbf{c} \qquad \text{and} \qquad \boldsymbol{\sigma} = \boldsymbol{\Sigma}\mathbf{c} \qquad (24)$$

where $\mathbf{u}$ and $\mathbf{v}$ contain the corresponding values of $u$ and $v$ from Eqs. (23), $\boldsymbol{\sigma} = \{\sigma_{xx}, \sigma_{yy}, \sigma_{xy}\}^T$ contains the corresponding values of $\sigma_{xx}, \sigma_{yy}$, and $\sigma_{xy}$ from Eqs. (22), $\mathbf{c}$ contains the $4N$ real coefficients $\mathbf{c} = \{a_{-N}, b_{-N} \ldots, a_{-1}, b_{-1}, a_1, b_1, \ldots, a_N, b_N\}^T$, the matrices $\mathbf{U}$ and $\mathbf{V}$ are real and rectangular coefficients matrices defined as

$$U(1,j) = 2\Re\left[p_1\zeta_1^k + p_2\left(C\zeta_2^k + B\zeta_2^{-k}\right)\right] \qquad (25a)$$

$$U(1,j+1) = 2\Im\left[-p_1\zeta_1^k + p_2\left(-C\zeta_2^k + B\zeta_2^{-k}\right)\right] \qquad (25b)$$

$$V(1,j) = 2\Re\left[q_1\zeta_1^k + q_2\left(C\zeta_2^k + B\zeta_2^{-k}\right)\right] \qquad (25c)$$

$$V(1,j+1) = 2\Im\left[-q_1\zeta_1^k + q_2\left(-C\zeta_2^k + B\zeta_2^{-k}\right)\right] \qquad (25d)$$

where $k = (j-1)/2 - N$ for $j = 1, 3, 5, \ldots, 2N-1$ and $k = (j+1)/2 - N$ for $j = 2N+1, 2N+3, \ldots, 4N-1$, and the matrix $\boldsymbol{\Sigma}$ is defined as

$$\Sigma_i(1,j) = (-1)^{i-1}2k\Re$$
$$\left[\mu_1^{i-1}\frac{\zeta_1^{k-1}}{\omega_1'(\zeta_1)} + \mu_2^{i-1}\frac{C\zeta_2^{k-1} - B\zeta_2^{-k-1}}{\omega_2'(\zeta_2)}\right] \qquad (26a)$$

$$\Sigma_i(1,j+1) = (-1)^{i-1}2k\Im$$
$$\left[-\mu_1^{i-1}\frac{\zeta_1^{k-1}}{\omega_1'(\zeta_1)} - \mu_2^{i-1}\frac{C\zeta_2^{k-1} + B\zeta_2^{-k-1}}{\omega_2'(\zeta_2)}\right] \qquad (26b)$$

where $i = 1(\boldsymbol{\Sigma}_{yy}), 2(\boldsymbol{\Sigma}_{xy})$, and $3(\boldsymbol{\Sigma}_{xx})$ and $\Im$ denotes the 'imaginary part' of a complex number. Furthermore, additional condition based on the overall equilibrium can be imposed. The resultant normal and shear forces from the induced stresses in a section should equal to the external applied loading,

$$F_n = \int \sigma_n \, dA \qquad \text{and} \qquad F_t = \int \sigma_t \, dA \qquad (27)$$

where $\sigma_n$ and $\sigma_t$ are the normal and tangential stresses, respectively, at the section and $F_n$ and $F_t$ are the normal and tangential force applied on the specimen. Knowing either $\mathbf{u}$, $\mathbf{v}$, or $\boldsymbol{\sigma}$ at various locations allows the best values of the unknown coefficients $\mathbf{c}$ to be determined in a least-squares sense.

#### 2.3.1 Determination of the unknown coefficients from displacements data

Suppose that the values of the in-plane displacement data, i.e., $u^*$ and $v^*$, are known, e.g., DIC, moiré, or speckle, at $m$ locations within the region $R_h^* \subseteq (R_z)_h$ and there are $q$ known boundary conditions (other than the traction-free boundary $\Gamma_0$) in terms of tractions, Eq. (1b), and/or displacements, Eq. (2b), conditions. The following system of simultaneous linear equations $\mathbf{A}\mathbf{c} = \mathbf{d}^*$ can be constructed such that the matrix $\mathbf{A}$ of size $(2m+q) \times 4N$ consists of the $m$ analytical expressions of each of the displacement components $\mathbf{u}^*$ and $\mathbf{v}^*$, Eqs. (23), and the $q$ expressions of the known stresses and/or displacements, the vector $\mathbf{c}$ has the $4N$ unknown real coefficients (defined previously), and the vector $\mathbf{d}^*$ includes the $2m$ known displacement values in addition to the known $q$ values of the boundary conditions such that $(2m+q) \gg 4N$. The best values of the coefficients $\mathbf{c}$, in a least-squares numerical sense, can be determined as

$$\mathbf{c} = \left(\mathbf{A}^T\mathbf{A}\right)^{-1}\mathbf{A}^T\mathbf{d}^* \qquad (28)$$

Once $\mathbf{c}$ is evaluated, the counterpart of the measured data, $\mathbf{d}^*$, can be evaluated as $\mathbf{d}_{\text{Airy}} = \mathbf{A}\mathbf{c}$. It is worth noting that one could use a single in-plane displacement field, rather than both components, to determine the unknown complex coefficients, $\mathbf{c}$.

### 2.3.2 Determination of the unknown coefficients from stress data

The unknown coefficients can also be determined from the known values of the stresses $\boldsymbol{\sigma}^*$, i.e., $\sigma_{xx}$, $\sigma_{yy}$, and $\sigma_{xy}$, from for example thermoelastic stress analysis and/or photoelastic stress analysis, at $m$ different locations such that the matrix $\mathbf{A}$ of size $(3m + q) \times 4N$ in this case consists of the $m$ analytical expressions of the stress components $\boldsymbol{\sigma}^*$, Eqs. (22), and the $q$ expressions of the known stresses and/or displacements, and the vector $\mathbf{d}^*$ includes the $3m$ known stress values in addition to the known $q$ values of the boundary conditions such that $(3m + h) \gg 4N$. Similarly, one also could use either the thermoelastic or photoelastic stress data to determine the complex coefficients.

### 2.3.3 Determination of the unknown coefficients from strain data

If the values of the strains, e.g., from strain gauges, are known, then the same procedure can be applied such that $\boldsymbol{\epsilon} = \mathbf{S}\boldsymbol{\sigma} = \mathbf{S}\boldsymbol{\Sigma}\mathbf{c}$ where $\mathbf{S} = \mathbf{C}^{-1}$ is the compliance matrix.

## 3 Inverse identification procedure

The proposed inverse identification procedure is based on minimizing the difference between the measured data, $\mathbf{d}^*$, in the region $R_h^*$ (in terms of displacements, strains, and/or stresses) with data constructed from Airy stress function, $\mathbf{d}_{\text{Airy}}^*$. The vectors $\mathbf{d}^*$ and $\mathbf{d}_{\text{Airy}}^*$ contain the values of the measured and reconstructed data, respectively, at the same spatial locations, where the experimental measurements represent the target values. Elastic constants are needed in CVM in order to calculate the $\mathbf{d}_{\text{Airy}}^*$. Therefore, assuming 1- and 2-axes are along the principal and transverse directions of material symmetry, the identification of elastic constants becomes a non-linear optimization problem formulated as

$$
\begin{aligned}
\min_{\mathbf{P}} \quad & \Lambda(\mathbf{P}) = \|\mathbf{r}^*\| = \|\mathbf{d}^* - \mathbf{d}_{\text{Airy}}^*\| \\
\text{subjected to} \quad & E_1 > E_2 \\
& 1 - v_{12}\sqrt{E_2/E_1} > 0 \\
& E_1^l \leq E_1 \leq E_1^u \\
& E_2^l \leq E_2 \leq E_2^u \\
& G_{12}^l \leq G_{12} \leq G_{12}^u \\
& v_{12}^l \leq v_{12} \leq v_{12}^u
\end{aligned}
\tag{29}
$$

where the error function $\Lambda$ is to be minimized and $\mathbf{P}$ is a vector containing the elastic constants, $E_1, E_2, G_{12}, v_{12}$, as optimization variables (the "$l$" and "$u$" superscripts denote the lower and upper bounds of elastic constants, respectively) and $\|\mathbf{r}^*\|$ is the norm of $\mathbf{r}^*$. The first two constraints in expression (29) ensure positive definiteness of the composite stiffness matrix and the remaining constraints define the lower and upper bounds of each of the elastic constants. Because Eq. (29) is nonlinear with respect to $\mathbf{P}$, iterative procedures are used for minimizing $\Lambda(\mathbf{P})$ and determining $\mathbf{P}$.

### 3.1 Procedure for identifying the elastic constants

For a loaded specimen to be characterized, the difference between the in-plane measured data, $\mathbf{d}^*$, in the region $R_h^* \subseteq (R_z)_h$ (no need to include free-traction boundary) and CVM predictions, $\mathbf{d}_{\text{Airy}}^*$, represented by the error function $\Lambda(\mathbf{P})$, Eq. (29), is minimized when the material elastic constants approach the values that produce specimen equilibrium. To perform the inverse identification procedure, the lower and upper bounds of the elastic constants, $\mathbf{P}^l$ and $\mathbf{P}^u$, must be initially specified. The spatial locations of the measured data $\mathbf{d}^*$ in the physical $z$-plane are mapped into the corresponding locations in the $\zeta$-plane using the mapping function, Eq. (14). Initial estimates of the elastic constants, $E_1^0, E_2^0, G_{12}^0, v_{12}^0$ within the lower and upper bounds of the design space, $\mathcal{D}$, are estimated. Recognizing that the complex coefficients, $A_k$, to be determined in the stress functions are fewer then the employed data, these unknown coefficients are evaluated in a least-squares sense, Eq. (28). Once the coefficients are determined, the counterpart image of the measured data, $\mathbf{d}_{\text{Airy}}^*$, can be constructed and the corresponding

difference with the measured quantity can be evaluated, $\mathbf{r}^* = \mathbf{d}^* - \mathbf{d}^*_{\text{Airy}}$. Furthermore, one can use the interior measured data $\mathbf{d}^*$ to determine the complex coefficients and use these determined coefficients to construct the image of the measured data $\mathbf{d}$ in the region $(R_z)_h$, and hence, the corresponding difference becomes $\mathbf{r} = \mathbf{d} - \mathbf{d}_{\text{Airy}}$. The new set of elastic constants is then determined using a numerical optimization technique. These processes must be repeated either for a certain specified number of iterations or until the maximum error between two consecutive results of the elastic constants is less than a user-defined stopping criteria,

$$\epsilon_a = \max_{\forall j}\left\{\left|\frac{\mathbf{P}^{i+1}(j) - \mathbf{P}^i(j)}{\mathbf{P}^{i+1}(j)}\right| \times 100\right\} < \epsilon_s$$

$$\text{where} \quad j = 1, 2, 3, 4 \tag{30}$$

Once the elastic constants are identified, the individual stresses, strains, and displacements throughout the region $(R_z)_h$, including along edge $(\Gamma_0)_h$, can be evaluated using Eqs. (22) and (23). A flowchart of the inverse identification procedure is depicted in Fig. 3.

### 3.2 Levenberg–Marquardt algorithm

For the current analysis, the Levenberg–Marquardt Algorithm (LMA) is used to minimize the cost function, $\Lambda(\mathbf{P})$, in Eq. (29) with respect to $\mathbf{P}$ in iterative procedures defined as

$$\mathbf{P}^{i+1} = \mathbf{P}^i - \left(\mathbf{J}^T\mathbf{J} + \lambda \cdot \text{diag}(\mathbf{J}^T\mathbf{J})\right)^{-1}\mathbf{J}^T\mathbf{r} \tag{31}$$

where $i$ is the iteration number, $\mathbf{J}$ and $\mathbf{J}^T$ are the Jacobian matrix and its transpose determined by backward finite-difference, $J_{m,n} = \partial r_m/\partial P_n$, where $m$ is the number of nodal data and $n$ is the number of elastic constants (4 in this work), and $\lambda$ is a non-negative damping factor. Two initial estimates of $\mathbf{P}$ are needed to calculate $\mathbf{J}$ and begin iterations. These two sets of the initial estimates, $\mathbf{P}^{-1} = \{E_1^{-1}, E_2^{-1}, G_{12}^{-1}, v_{12}^{-1}\}^T$ and $\mathbf{P}^0 = \{E_1^0, E_2^0, G_{12}^0, v_{12}^0\}^T$, are evaluated from the following design space $\mathcal{D}$,

$$\mathbf{P}^k = (\mathcal{E}_l + (\mathcal{E}_u - \mathcal{E}_l)R_i)\mathbf{P}^T \qquad \text{where} \quad k = -1, 0 \tag{32}$$

where $\mathcal{E}_l$ and $\mathcal{E}_u$ are the minimum and maximum absolute random errors (user specified), respectively, $R_i$ is an independent generated random number

$(0 \leq R_i \leq 1, i = 1, 2, 3, 4)$ and $\mathbf{P}^T = \{E_1, E_2, G_{12}, v_{12}\}^T$ are the reference (target) elastic constants. A random number generated in MATLAB program $^{®}$ (Mathworks, Inc., 2019) is used to generate the $R_i$ independently for each input $k$. Therefore, the initial estimates based on Eq. (32) are generated randomly assuming a uniform probability distribution over the domain $\mathcal{D}$. For instance if $\mathcal{E}_l = 0$ and $\mathcal{E}_u = 3$, then the initial estimates, $\mathbf{P}^{-1}$ and $\mathbf{P}^0$, are at most $3 \cdot \mathbf{P}^T$ (with $(\mathcal{E}_u - 1) \times 100\% = 200\%$ difference error) and at least $0 \cdot \mathbf{P}^T$ (with $(\mathcal{E}_l - 1) \times 100\% = -100\%$ difference error) from the target values.

A new set of elastic constants, $\mathbf{P}^{i+1}$, is determined from Eq. (31), and validated against the constraints in Eq. (29). The validated $\mathbf{P}^{i+1}$ is used as input to the new analysis, and the resulting $\mathbf{d}_{\text{Airy}}$ is used to determine $\Lambda_{i+1}$. If $\Lambda_{i+1} < \Lambda_i$, then the elastic constants are updated, $\mathbf{P}^{i+1} \rightarrow \mathbf{P}^i$, $\lambda$ is increased by a factor of 5, and the next iteration begins. If $\Lambda_{i+1} > \Lambda_i$, then $\lambda$ is reduced by a factor of 2 and $\mathbf{P}^i$ is not updated. The cost function decreases as the identified elastic constants produced a measured field, $\mathbf{d}_{\text{Airy}}$, that approaches the experimental field, $\mathbf{d}$. Figure 4 illustrates the flowchart of the proposed inverse method based on CVM and LMA.

The proposed inverse identification method depends on many factors, including but not limited to (1) the amount and locations of the employed data, $m$, in the region of interest, $R_h^*$, (2) the amount of the additional employed boundary conditions, $q$, (3) the number of retained terms, $N$, in the stress function, (4) the initial estimates used to compute $\mathbf{J}$ and how far these estimates from the target values, $\mathcal{E}_u$ and $\mathcal{E}_l$, (5) the stopping criteria, $\epsilon_s$, and/or the maximum number of iterations, and (6) the damping factor, $\lambda$, in Eq. (31).

## 4 Simulation experiment

The proposed inverse identification method is tested using in-plane displacement components of a loaded finite-width glass/epoxy tensile orthotropic composite as shown in Fig. 5 with a centrally located circular hole (radius $R = 1.745$ cm). The loading is applied horizontally ($x$-axis) by a uniform tensile stress, $\sigma_0$, and is along the strong/stiff (principal) material orientation (1-axis). The mechanical properties are $E_1 = 34.2$ GPa, $E_2 = 14.1$ GPa, $G_{12} = 3.4$ GPa, and
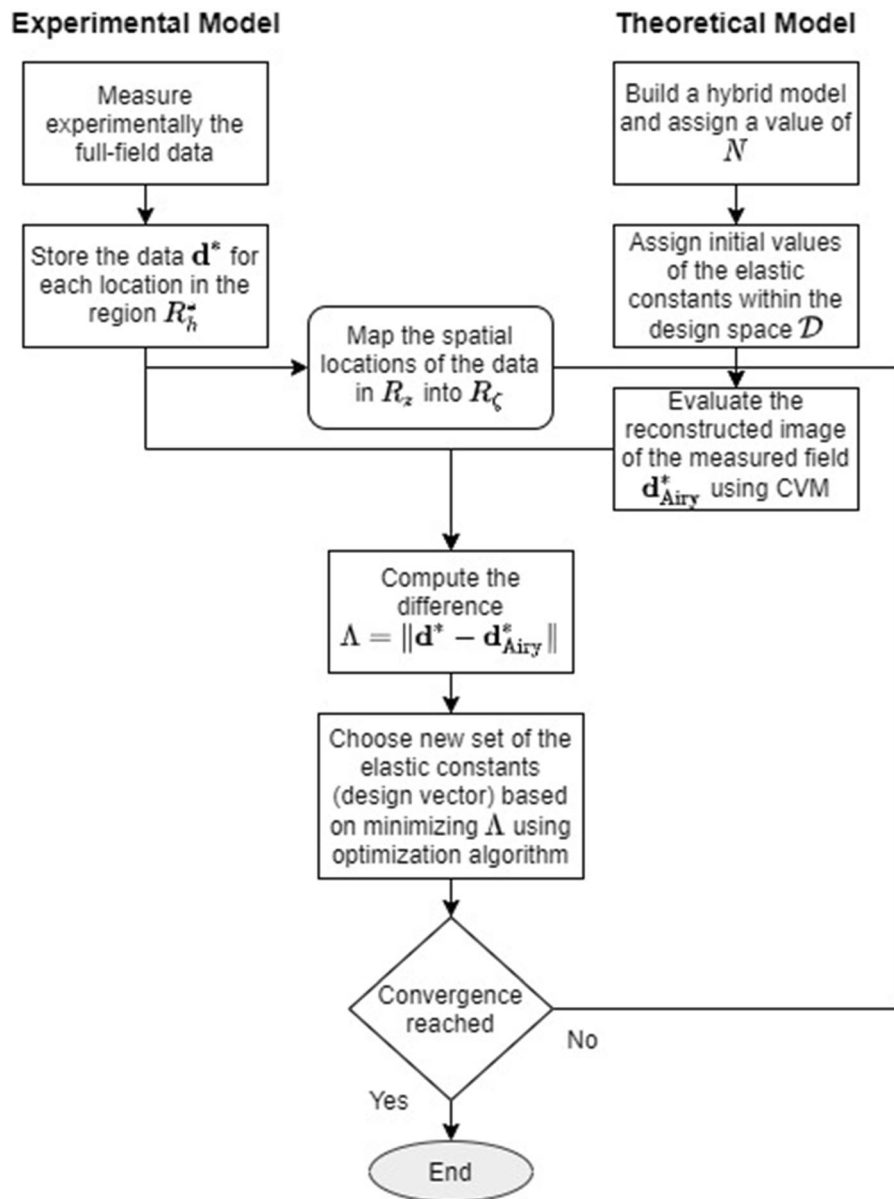
**Fig. 3** Flowchart for material identification using CVM

$v_{12} = 0.22$, and the overall laminate dimensions are $L = 43.2$ cm long, $W = 7.13$ cm wide ($W/R = 4.08$) and $t = 3.45$ mm thick. The coordinate system origin is at the center of the plate, and the response is symmetric about the $x$- and $y$-axes. Because of symmetry, one quarter of the plate was used to provide the in-plane displacement data. The simulation was conducted to test the reliability of the proposed scheme by adding zero-mean Gaussian white noise to the FEM-determined displacements. For subsequent analyses,

symmetrical boundary conditions along discrete points in the $x$- and $y$-axes were employed ($q = 0.1m$), the load equilibrium at the line $x = 0$ was enforced [Eq. (27)], $\epsilon_s$ was set to 0.1%, and $\lambda$ was initially set to 1 and adjusted according to Eq. (31).

The in-plane input displacement values, $\mathbf{u}^*$ and $\mathbf{v}^*$, for determining the elastic constants are located in the region $1.02 < r/R < 1.60$, where $r$ is the radial distance from the hole center. FEM displacements were deteriorated using zero-mean Gaussian white noise
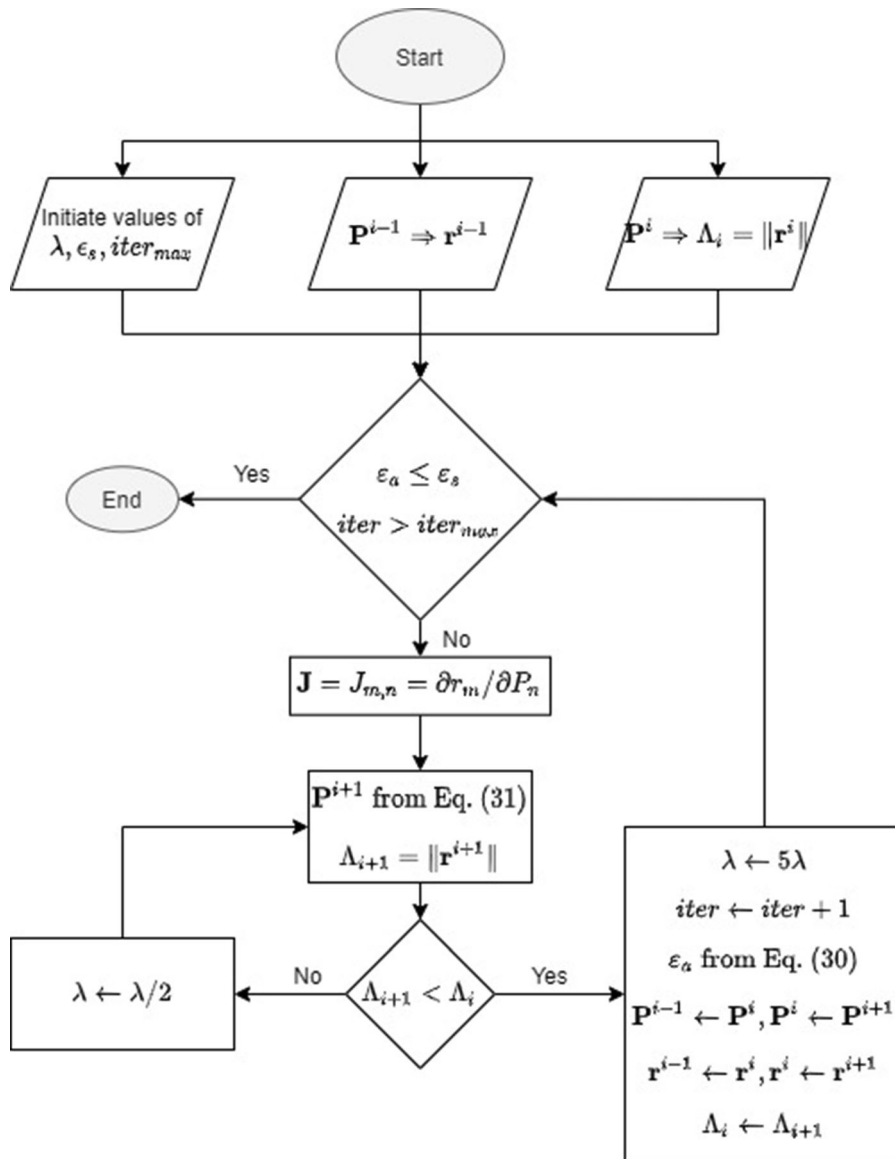
**Fig. 4** Flowchart of the proposed inverse method based on CVM and LMA

in order to simulate the associated errors in the experimental measurements,

$$u_i = u_{t,i} + \mathcal{N}(0,\gamma)u_{t,i} \quad \text{and} \quad v_i = v_{t,i} + \mathcal{N}(0,\gamma)v_{t,i}$$
$$(33)$$

where $u_i$, $v_i$ and $u_{t,i}$, $v_{t,i}$ are the noisy and predicted FE simulated in-plane displacement components, respectively, and $\mathcal{N}(0,\gamma)$ is the standard Gaussian function with a mean of 0 and standard deviation of $\gamma$. Figure 6 shows the noisy displacement field with $\gamma = 5\%$ and the numerically predicted field from the FEA.

The proposed inverse procedure can be generally described as the iterative adjustments of the design parameters (elastic constants) in a numerical model (CVM) to minimize the cost function (via LMA) represented as the difference between the measured quantity (displacement) and its counterpart evaluated numerically. To demonstrate the effectiveness of the proposed inverse technique on identifying the elastic constants, the effects of the superimposed noise, $\gamma$, to the simulated displacement data, the number of employed data, $m$, and the number of retained real
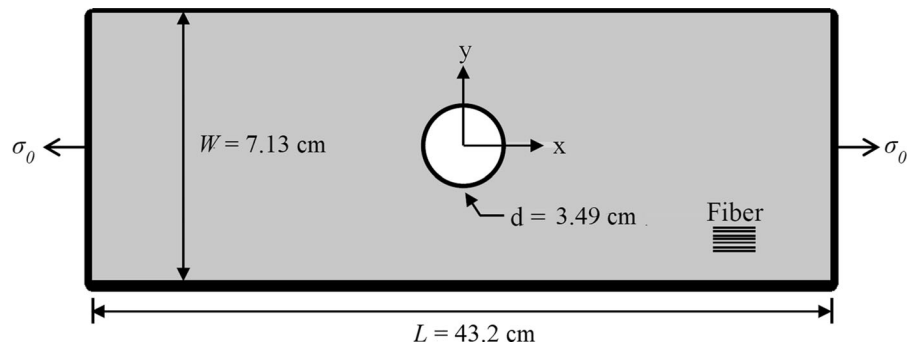
**Fig. 5** Finite width uniaxially loaded [0/90/0$_{10}$/90/0] glass/epoxy orthotropic composite plate containing a circular hole
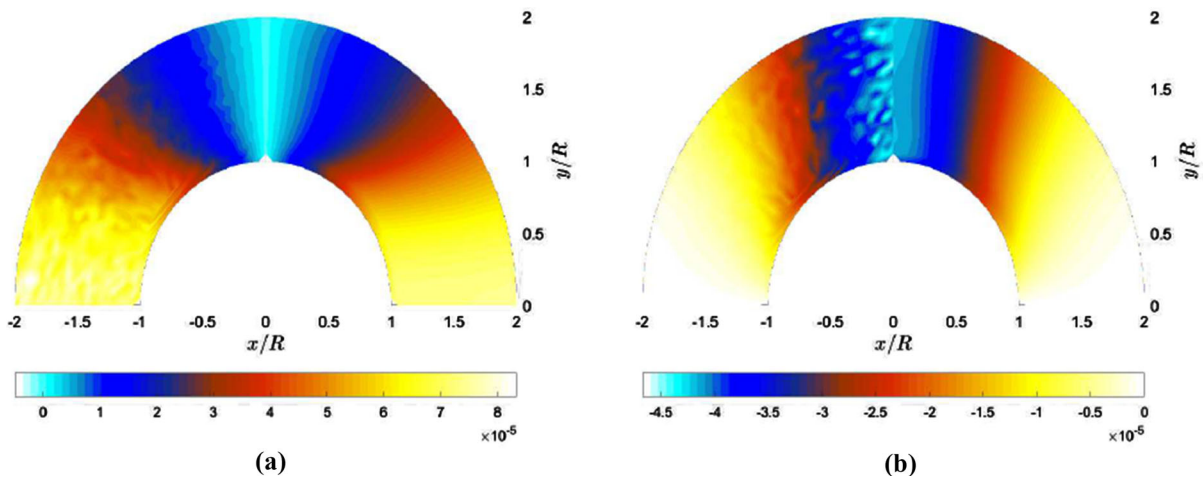


**Fig. 6** The noisy displacement field with $\gamma = 5\%$ (left) and the numerically predicted displacement field from the FEA (right); **a** $u$- and **b** $v$-displacement fields

coefficients in the stress function, $4N$, are considered in the following subsections.

4.1 Effects of uncertainties in the elastic constants

To assess the uncertainties in the mechanical property identification, a Monte Carlo method is used to generate $k$ sets of elastic constants from a normal distribution with mean corresponding to the target values and a covariance of $CV$ and evaluate the reconstructed displacement field. For illustration, $N = 13$ terms were retained, $\gamma = 5\%$ is used, and $k = 1000$ sets of elastic constants are generated from a normal distribution with a mean corresponding to the target value and a covariance $CV$ that varies from 0 to 15% for all the elastic constants. The reconstructed displacement field is compared with the numerically predicted displacement field from the FEA without

any additional noise scatter (corresponding to the case of $\gamma = 0$). The normalized norm errors for the in-plane displacement field are shown in Fig. 7 when employing different number of data that are randomly generated from the region $R^*$ adjacent to the circular hole. It is clear that the errors are reduced when employing large numbers of data when the covariance is less than 10%. This indicates that the CVM more accurately predicts the displacement field when a large number of data is employed. The CVM becomes sensitive to the variation of the elastic constants when the standard deviations are 10% away from the mean values. The larger the deviations of the elastic constant are, the larger the variation from the predicted displacement field with corrected field becomes. The error associated with the $u$-displacement is small compared to the error associated with $v$-displacement because the load was applied along the $x$-direction.
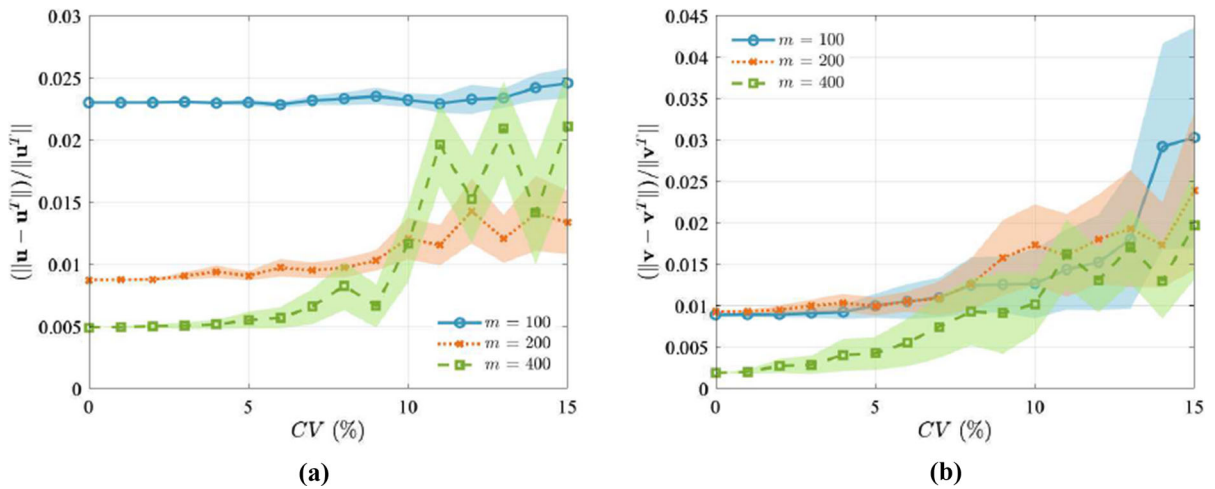
**Fig. 7** The normalized norm error in **a** $u$- and **b** $v$-displacement field with presence of uncertainties in the elastic constants

### 4.2 Assessing the effect of the initial parameter estimates

LMA is a gradient-based optimizing method that depends on two sets of the initial estimates, $\mathbf{P}^{-1}$ and $\mathbf{P}^0$. Therefore to assess the effects of the initial estimates on the convergence of the proposed inverse method and to find the global minimum, different initial estimates are randomly generated from the design space $\mathcal{D}$ given by Eq. (32) to determine several elastic constants. Their averages are subsequently used as the first initial estimates, $\mathbf{P}^{-1}$, for the next test run where $\mathbf{P}^0$ are generated from another random set from the design space $\mathcal{D}$. These processes are repeated until each set of elastic constants converges. The range of the design space could be further narrowed by setting the identified ranges (mean $\pm$ standard deviation) as the upper and lower bounds of the initial estimates.

A virtual experiment is conduced using $4N = 28$ retained real coefficients, $m = 800$ in-plane displacement data, one set of $\mathbf{P}^{-1}$, and $k = 100$ sets of $\mathbf{P}^0$ generated from Eq. (32) with $\mathcal{E}_l = 0.1$ and $\mathcal{E}_u = 4.0$. The average of identified parameters of the 100 sets are used as the initial guess $\mathbf{P}^{-1}$ for the next run where another 100 sets of $\mathbf{P}^0$ are generated. The convergence rates with white noise error of $\gamma = 0$ (no superimpose error) and 5% are shown in Figs. 8 and 9, respectively. The solid line represents the determined averages, and the shaded area represents the corresponding standard deviation for each of the 100 sets. The inverse method

when using the FEM-simulated displacement field correctly identifies the elastic constants, which demonstrates the reliability of the method. For noisy simulated data, the identified elastic constants have a coefficient of variation that is less than 1% and their averages are within 10% from the target values. The results of Fig. 9 demonstrate the effectiveness of the inverse method in determining the elastic constants regardless how noisy the implemented data are and how far the initial guesses are from the target values. The method converges irrespective of proximity of initial guesses to the target values.

The inverse method more accurately identified $E_1$ compared to the other elastic constants. This is not surprising because the far field displacement is dominated by $E_1$. If higher data density could be used as per Fig. 7, better estimates of the transverse constants would be obtained. For the subsequent analyses, the target values will be used as the first initial guess, $\mathbf{P}^{-1}$, while $k = 100$ sets of $\mathbf{P}^0$ will be generated from the design space $\mathcal{D}$ with $\mathcal{E}_l = 0.1$ and $\mathcal{E}_u = 2.0$.

### 4.3 Assessing the effect of the superimposed noise

The superimposed noise is quantified by the standard deviation, $\gamma$, of the Gaussian function in Eq. (33). The effects of increasing the simulated noise scatter on the identified elastic constants are shown in Fig. 10 when retaining $4N = 28$ real coefficients and using different amounts of employed data. For input displacement
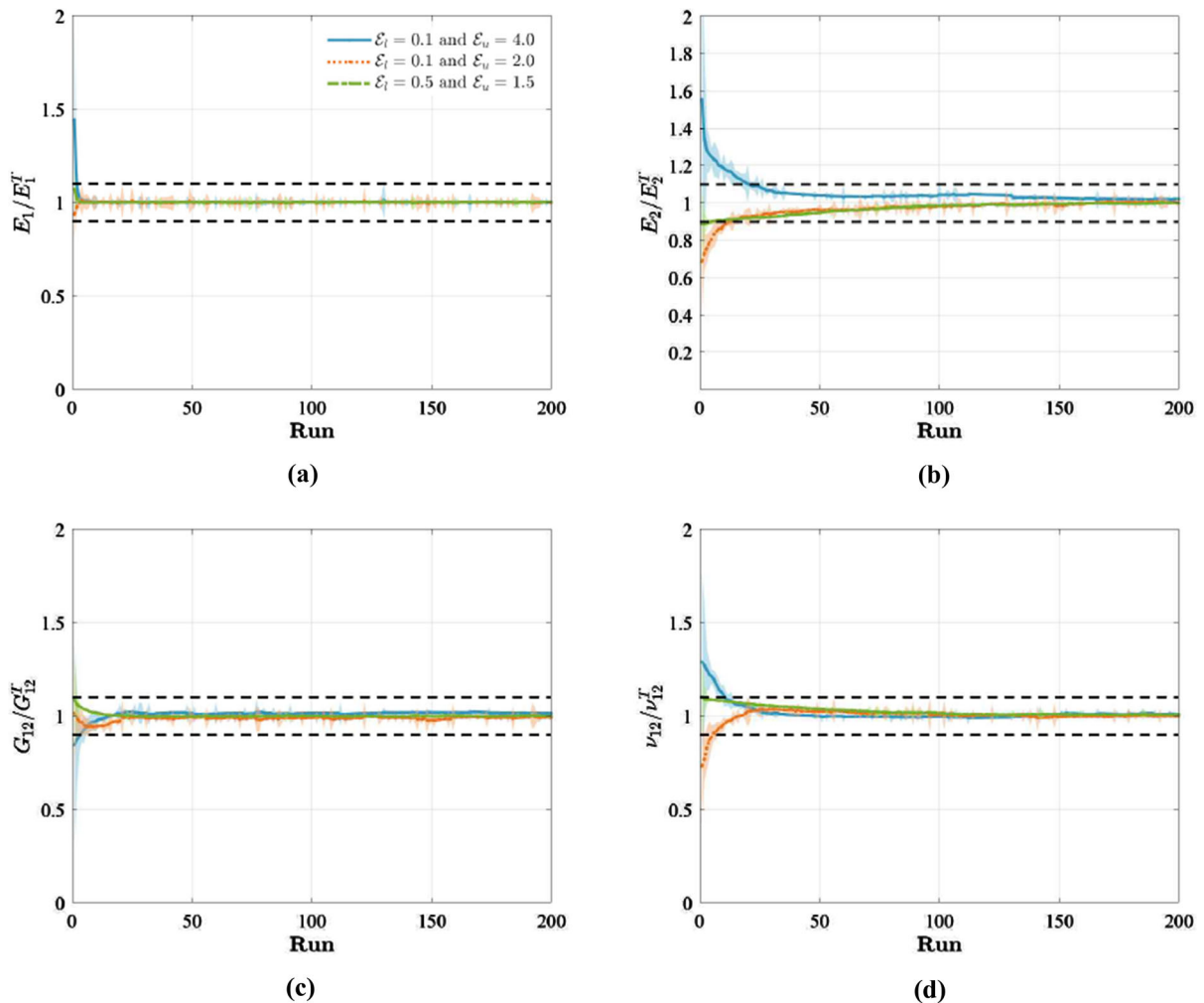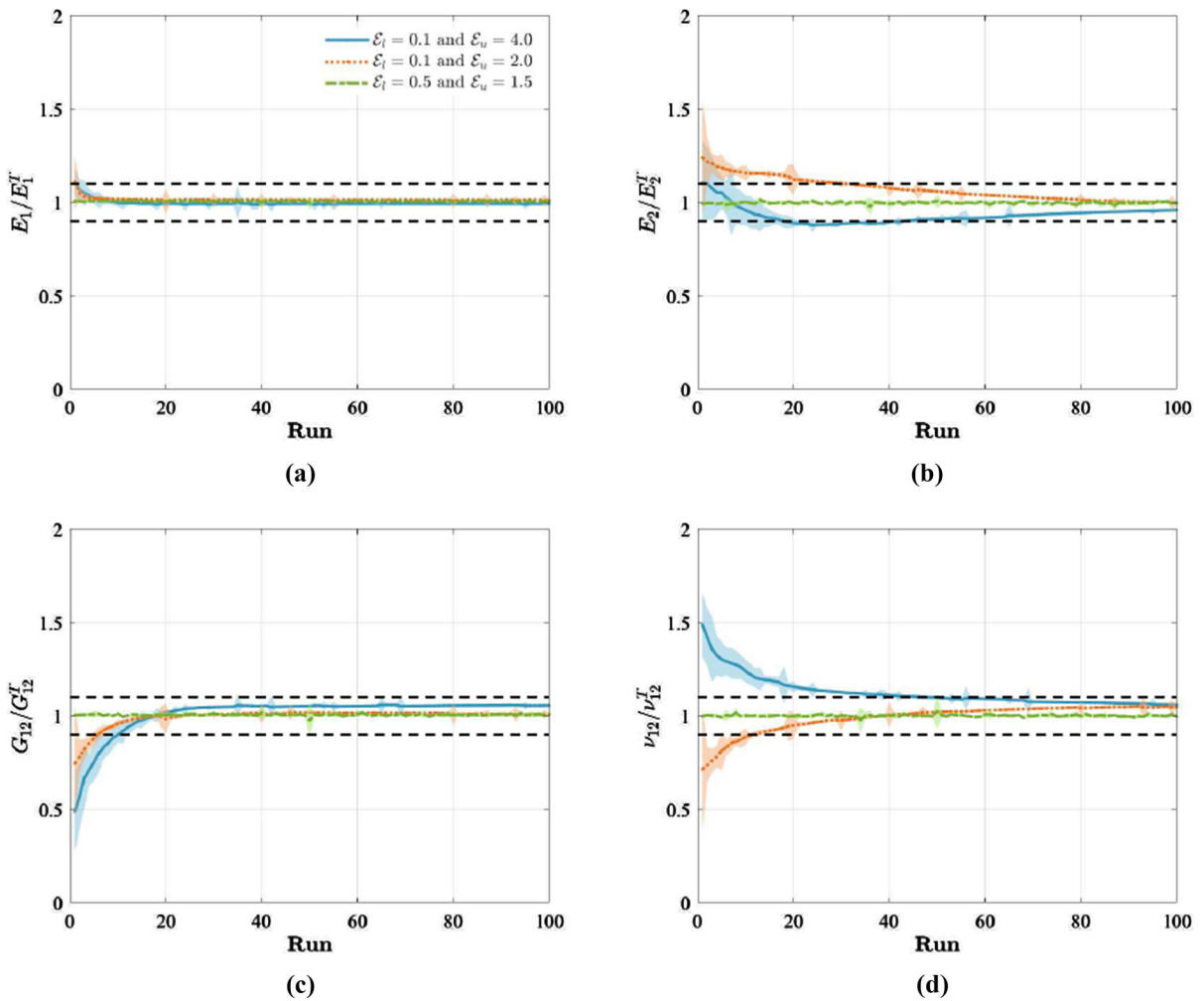
**Fig. 8** The convergence of the inverse method for **a** $E_1$, **b** $E_2$, **c** $G_{12}$, and **d** $v_{12}$ using the numerically predicted FEM displacement components and different ranges of the initial guesses, $\mathcal{E}_l$ and $\mathcal{E}_u$

data without imposing noise scatter, i.e., $\gamma = 0$, the identification of the elastic constants is very close to the target values regardless of the number of employed data and the initial guesses. As expected, the discrepancy between the identified and target values increases with the increases in the superimposed noise scatter. When employing the in-plane displacement components using $m = 200$ data points or less, the inverse procedure gives reasonable results when the standard deviation of the superimposed noise is less than $\gamma = 5\%$. In contrast, the averages of the identified elastic constants are within 10% from the input values when using at least 400 data points.

### 4.4 Effect of the number of retained real coefficients

Using different number of employed $m$ 'noisy' input displacement values with $\gamma = 5\%$, the average of normalized identified elastic constants with respect to the target values for different numbers of retained real coefficients $4N$ are illustrated in Fig. 11. The discrepancy of the identified elastic constants was increased with increases in the number of retained coefficients due to the increasing in the condition number of the matrices $\mathbf{U}$ and $\mathbf{V}$ in Eq. (25). Retaining 20 to 32 real coefficients is appropriate for determining the elastic constants. In general, the coefficients of variation were reduced when employing large numbers of
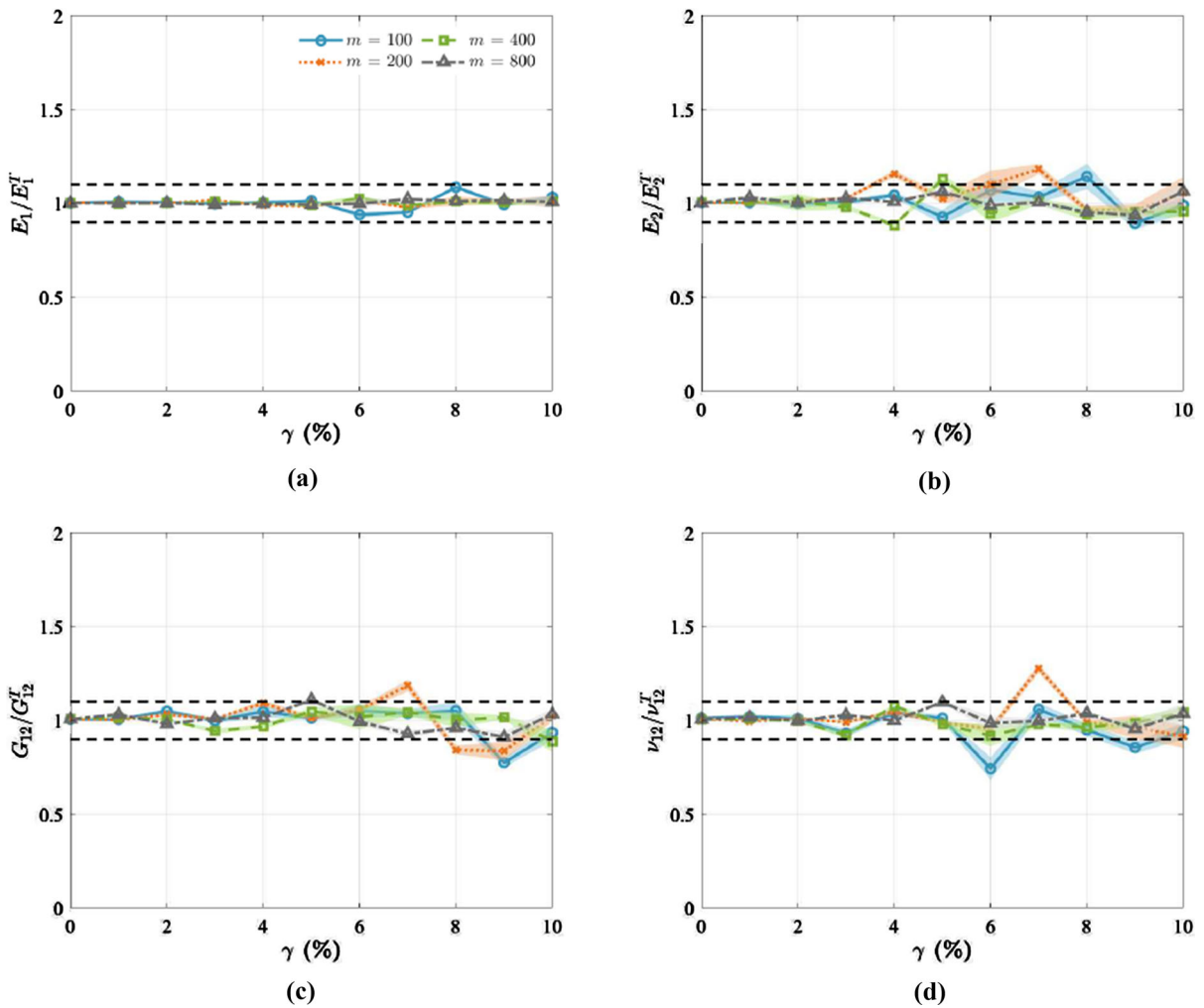
**Fig. 9** The convergence of the inverse method for **a** $E_1$, **b** $E_2$, **c** $G_{12}$, and **d** $\nu_{12}$ components with $\gamma = 5\%$ and different ranges of the initial guesses, $\mathcal{E}_l$ and $\mathcal{E}_u$

displacement data. Giving the fact that only $m = 800$ displacement data were processed in the inverse scheme, $E_1$ was accurately identified compared to other elastic constants.

### 4.5 Sensitivity to random noise

The reliability of the inverse method deteriorates with the increasing noise. In practice, only one level of noise is present. While random noise is generally constant, systematic noise can be controlled (to a certain extent) by apparatus setup and operator diligence. Here we illustrate the effect of noise with different noise levels without specification of a particular data type, e.g., DIC, TSA, strain gauges,

etc. Even though the inverse procedure does not require the use of the full-field displacement data, the accuracy of the identification is improved with the increasing in the number of employed data close to the hole boundary where the heterogeneous displacement field is present. To further investigate the sensitivity of the method with the increases of the random superimposed noise, the error maps of the absolute true percentage relative error between the predicted and target values are shown in Fig. 12. Percentage error for the identified values of $E_1$ is relatively small compared to the other identified elastic constants. The method identifies properly the elastic properties up to 7% noise level when employing large number of displacement data. Accurate identification of elastic

**Fig. 10** The convergence of the inverse method for **a** $E_1$, **b** $E_2$, **c** $G_{12}$, and **d** $v_{12}$ with different noise levels, $\gamma$

constants is obtained for a noise level less than 4% when employing relatively few displacement data.

## 5 Strain input data

Having substantiated the robustness of the inverse scheme, the practicality of the method is demonstrated using strain gauge measurements. A loaded perforated plate with geometry shown in Fig. 5 and made of glass/epoxy composite was tested by Baek and Rowlands [22]. Strain data and their spatial locations are listed in Table 1.

The measured strain data ($\epsilon_{xx}$, $\epsilon_{yy}$, and $\epsilon_{xy}$) at four locations ($m = 12$) were used to identify the elastic

properties. As with the simulated experiment, $k = 100$ sets of $\mathbf{P}^{-1}$ and $\mathbf{P}^0$ are generated from Eq. (32) with $\mathcal{E}_l = 0.01$ and $\mathcal{E}_u = 4.0$. The averages of these identified elastic properties are used as the initial estimate $\mathbf{P}^{-1}$ for the next step where another 100 sets of $\mathbf{P}^0$ were generated. The convergence rates using $N = 1$ are shown in Fig. 13a. The corresponding means and standard deviations of the identified elastic constants are $E_1 = 33.67 \pm 0.33$ GPa, $E_1 = 13.83 \pm 0.28$ GPa, $G_{12} = 3.962 \pm 0.040$ GPa, and $v_{12} = 0.198 \pm 0.0147$ GPa. Irrespective of how far the initial guesses are from the actual values, the identified elastic constants (except $G_{12}$) are within 10% of the elastic values determined from tensile tests. Figure 13a addresses the real possibility of not
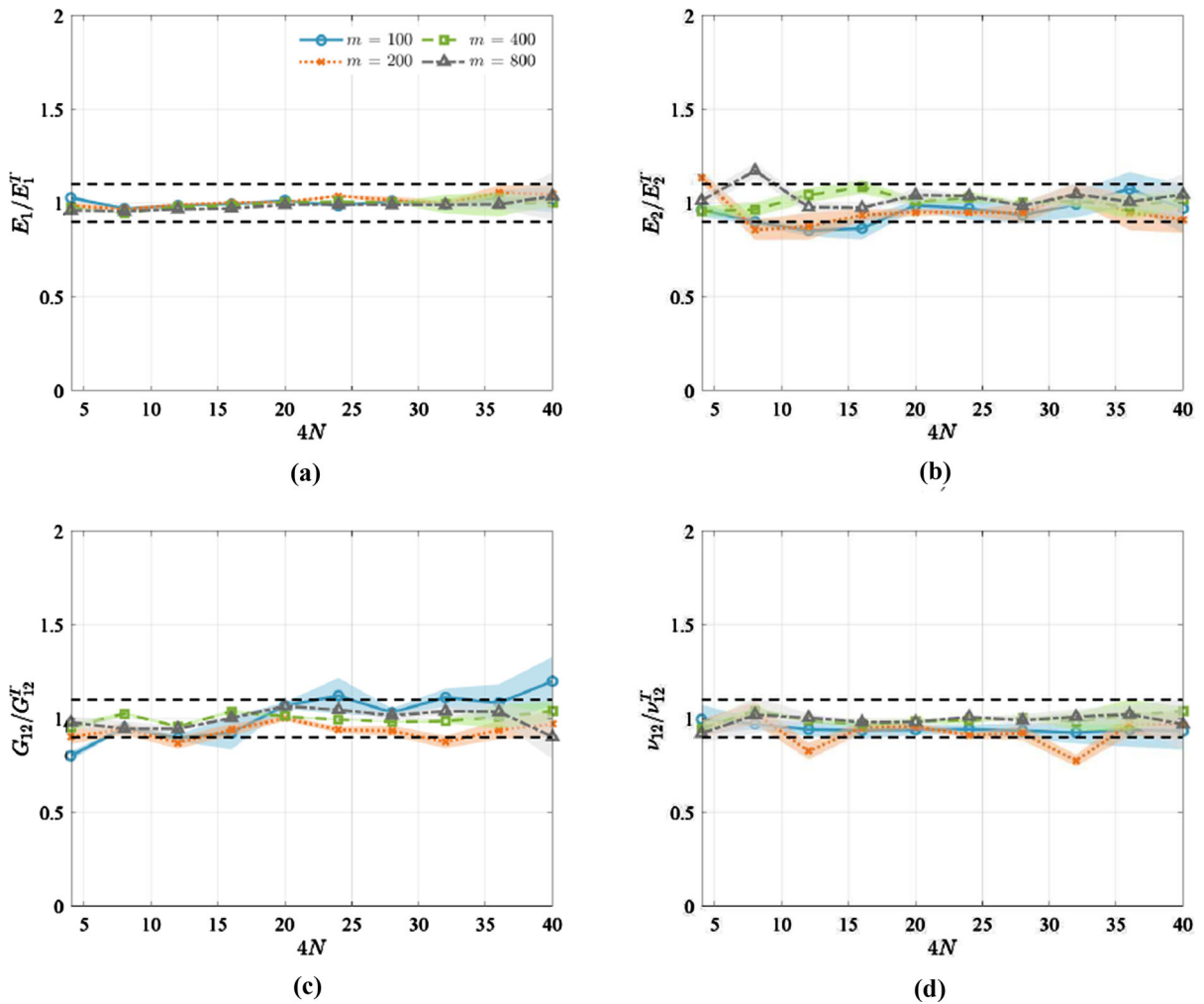
**Fig. 11** The convergence of the inverse method for **a** $E_1$, **b** $E_2$, **c** $G_{12}$, and **d** $v_{12}$ using different numbers of retained real coefficients, $4N$, and employed data, $m$

knowing a priori what the elastic constants are, and by assuming any initial estimates, the method will eventually converge to the mean elastic constants of the tested material.

To demonstrate that the identified elastic constants from the inverse procedure provided the optimum value in terms of the objective functional $\Lambda(\mathbf{P})$, Fig. 13b illustrates that the cost function when using the identified constants is less than the cost function when using the elastic constants determined from tensile tests. Experimental advantages of the proposed hybrid inverse method are that few terms are retained in the stress function representation and relatively few arbitrarily located measured input data are needed. Therefore, the input data locations can be selected

according to the user's desire and can be originated away from the discontinuity of concern. This can be advantageous because regions of unreliable or sparse experimental information can be avoided. For example, if source of input data is full-field such as digital image correlation, thermoelastic, photoelastic, moiré, or speckle, then regions of good and bad source data would typically be apparent and the investigator could act accordingly. Also, as previously stated, the method does not necessitate knowing the entire boundary and distant loading conditions.

The results indicate that the presented inverse method is able to accurately identify the elastic constants of the material under investigation. The simplicity and ease of implementing the proposed
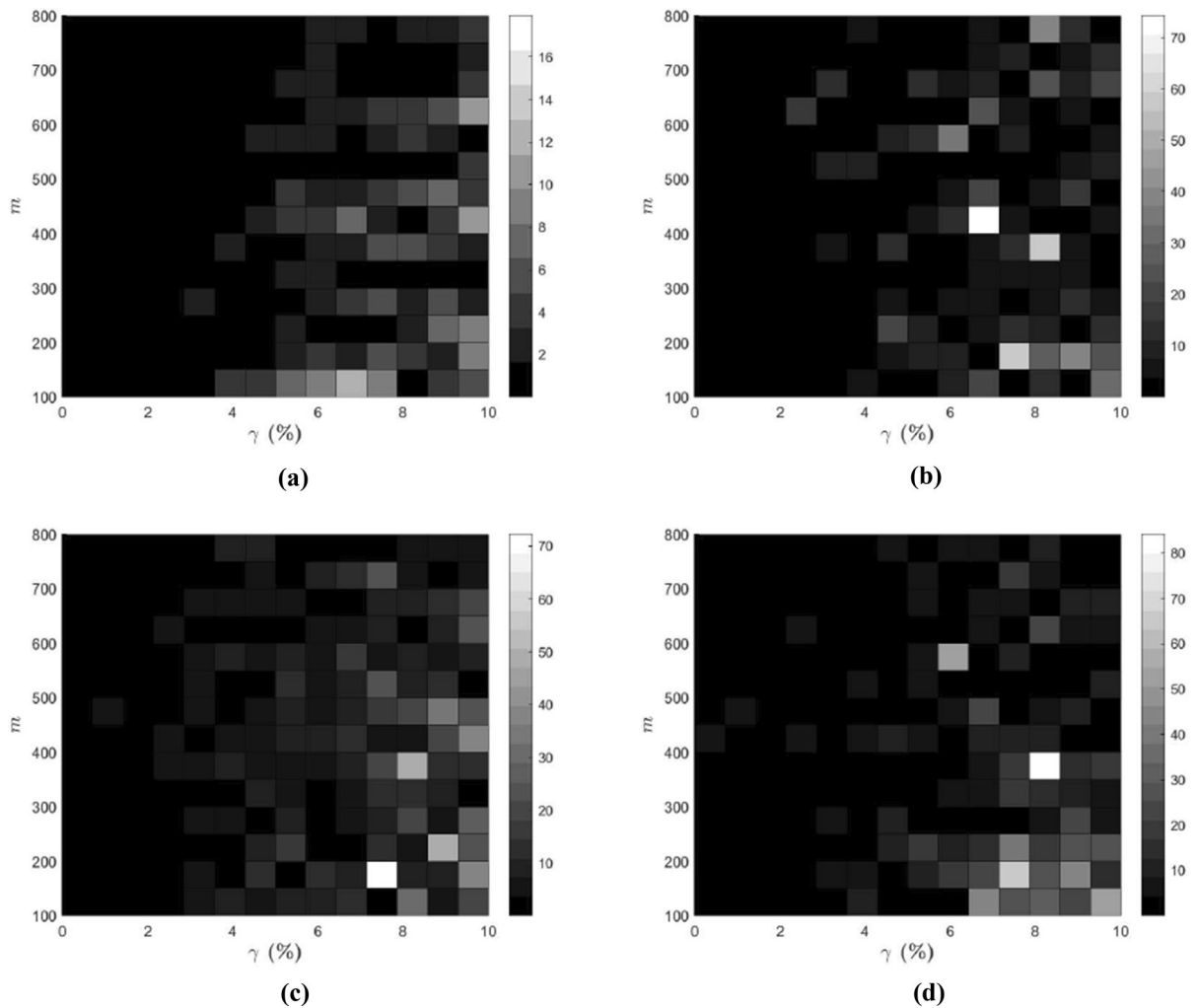
**Fig. 12** The error maps of the absolute true percent relative error for **a** $E_1$, **b** $E_2$, **c** $G_{12}$, and **d** $v_{12}$

**Table 1** Measured strain (stress) components and their locations for an applied stress of 25.38 MPa from reference [22]

| Location | Coordinates | | Strain components ($\mu\epsilon$) | | |
|---|---|---|---|---|---|
| | $x/R$ | $y/R$ | $\epsilon_{xx}$ | $\epsilon_{yy}$ | $\epsilon_{xy}$ |
| 1 | 2.9675 | 1.0260 | 838 | − 112 | − 910 |
| 2 | 2.9481 | 0.0325 | 424 | 32 | 0 |
| 3 | 2.0682 | 1.0292 | 898 | − 100 | − 1197 |
| 4 | 2.0455 | 0.0325 | 237 | − 65 | 0 |

inverse method render it convenient for experimental analysis. The present scenario involves a circular hole (whose mapping function is readily available) and

displacement and strain input data, but the method is applicable to various-shaped discontinuities and different input experimental data. Once the elastic constants are identified, CVM can be used to smooth the original input data, enhance the edge information, and determine the individual stresses, strains, and displacements throughout, including on the edge of the hole or cutouts, even though no experimental data were used there [15–17, 20–23].

## 6 Conclusions

A new, efficient hybrid inverse method for in-plane material stiffness identification of perforated
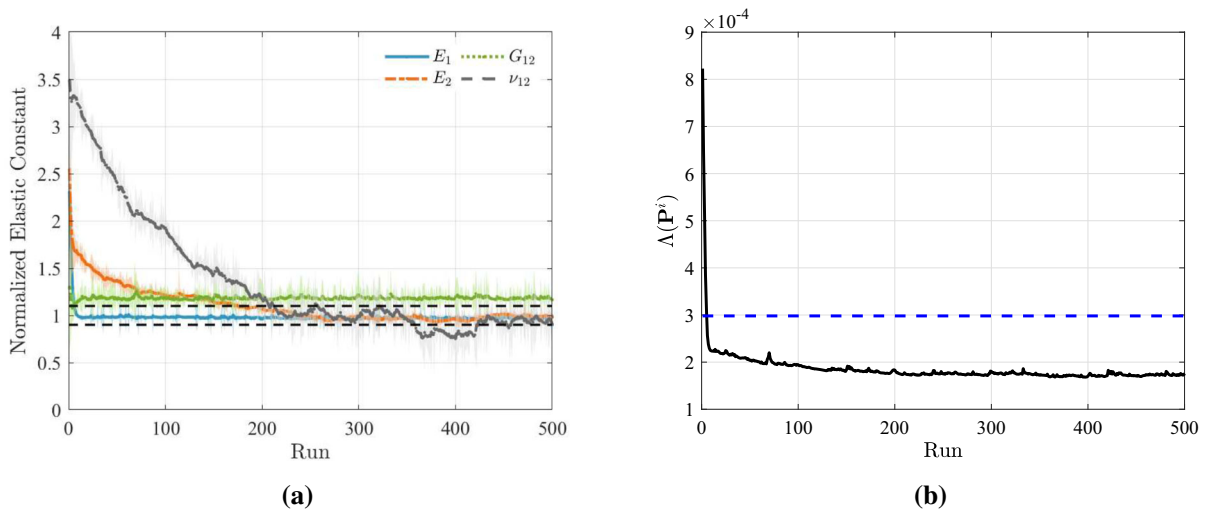
**Fig. 13** **a** The convergence of the inverse method for the four elastic properties and **b** the fitness value of the cost function $\Lambda(\mathbf{P}^i)$ when using measured strain data with $N = 1$, and $\mathcal{E}_l = 0.01$ and $\mathcal{E}_u = 4.0$

composite geometry was presented. The method is based on minimizing the experimental quantity (simulated in-plane displacement components superimposed with random noise and measured strain data were used here) located in a region adjacent to a traction-free boundary with its counterpart obtained using CVM. LMA was used to minimize the cost function where the elastic constants were the design parameters. The effects of increasing the magnitude of the zero-mean Gaussian noise and the number of employed data on the accuracy and consistency of the predicted elastic constants were demonstrated. The accuracy and variability of the identified elastic constants deteriorated with the increasing in the noise level. Identified elastic constants were within 10% of the actual constants when the simulated noise magnitude had standard deviation less than 10%, which is quite reasonable in practice.

**Declarations**

**Conflict of interest** The authors declare that there is no conflict of interest.

## References

1. Grédiac M (2004) The use of full-field measurement methods in composite material characterization: interest and limitations. Compos Part A Appl Sci Manuf 35:751–761
2. Le Magorou L, Bos F, Rouger F (2002) Identification of constitutive laws for wood-based panels by means of an inverse method. Compos Sci Technol 62(03):591–596
3. Genovese K, Lamberti L, Pappalettere C (2004) A new hybrid technique for in-plane characterization of orthotropic materials. Exp Mech 44:584–592
4. Molimard J, Le Riche R, Vautrin A, Lee JR (2005) Identification of the four orthotropic plate stiffnesses using a single open-hole tensile test. Exp Mech 45:404–411
5. Seon G, Makeev A, Cline J, Shonkwiler B (2015) Assessing 3d shear stress–strain properties of composites using digital image correlation and finite element analysis based optimization. Compos Sci Technol 117:371–378
6. Seon G, Makeev A, Schaefer JD, Justusson B (2019) Measurement of interlaminar tensile strength and elastic properties of composites using open-hole compression testing and digital image correlation. Appl Sci 9:2647
7. Geymonat G, Pagano S (2003) Identification of mechanical properties by displacement field measurement: a variational approach. Meccanica 38(5):535–545. https://doi.org/10.1023/A:1024766911435
8. Guchhait S, Banerjee B, Alla J (2018) Thermo-elastic material parameters identification using modified error in constitutive equation approach. Inverse Probl Sci Eng 26:1356–1382
9. Syed-Muhammad K, Toussaint E, Grédiac M, Avril S, Kim J (2008) Characterization of composite plates using the virtual fields method with optimized loading conditions. Compos Struct 85:70–82

10. Rossi M, Pierron F (2012) On the use of simulated experiments in designing tests for material characterization from full-field measurements. Int J Solids Struct 49:420–435

11. Avril S, Pierron F (2007) General framework for the identification of constitutive parameters from full-field measurements in linear elasticity. Int J Solids Struct 44:4978–5002

12. Avril S, Bonnet M, Bretelle A-S, Grédiac M, Hild F, Ienny P, Latourte F, Lemosse D, Pagano S, Pagnacco E, Pierron F (2008) Overview of identification methods of mechanical parameters based on full-field measurements. Exp Mech 48:381

13. Alshaya A, Considine JM, Rowlands R (2018) Determination of constitutive properties in inverse problem using airy stress function. In: Residual stress, thermomechanics and infrared imaging, hybrid techniques and inverse problems, volume 8: proceedings of the 2017 annual conference on experimental and applied mechanics. Springer, pp 73-81

14. Alshaya A, Considine JM (2019) Determination of constitutive parameters in inverse problem using thermoelastic data. In: Baldi A, Quinn S, Balandraud X, Dulieu-Barton JM, Bossuyt S (eds) Residual stress, thermomechanics and infrared imaging, hybrid techniques and inverse problems, vol 7. Springer, Berlin, pp 25–34

15. Lin ST, Rowlands RE (1995) Thermoelastic stress analysis of orthotropic composites. Exp Mech 35:257–265

16. Rhee J, Rowlands R (1999) Thermoelastic-numerical hybrid analysis of holes and cracks in composites. Exp Mech 39:349–355

17. Alshaya A, Shuai X, Rowlands R (2016) Thermoelastic stress analysis of a finite orthotropic composite containing an elliptical hole. Exp Mech 56:1373–1384

18. Alshaya A, Lin S-J (2019) Hybrid stress analysis of a near-surface circular hole in finite structures. Proc Inst Mech Eng Part C J Mech Eng Sci 234:1366–1381

19. Kalaycioglu B, Alshaya A, Rowlands R (2019) Experimental stress analysis of an arbitrary geometry containing irregular shaped hole. Strain 55:e12306

20. Hawong JS, Lin CH, Lin ST, Rhee J, Rowlands RE (1995) A hybrid method to determine individual stresses in orthotropic composites using only measured isochromatic data. J Compos Mater 29:2366–2387

21. Baek TH, Rowlands RE (1999) Experimental determination of stress concentrations in orthotropic composites. J Strain Anal Eng Des 34:69–81

22. Baek T, Rowlands R (2001) Hybrid stress analysis of perforated composites using strain gages. Exp Mech 41:195–203

23. Alshaya A, Rowlands R (2017) Experimental stress analysis of a notched finite composite tensile plate. Compos Sci Technol 144:89–99

24. Savin GN (1961) Stress concentration around holes. Pergamon Press, Oxford

25. Lekhnitskii SG (1963) Theory of elasticity of an anisotropic elastic body, 1st edn. Holden-Day, San Francisco

26. Gerhardt TD (1984) A hybrid/finite element approach for stress analysis of notched anisotropic materials. J Appl Mech 51:804–810

27. Bowie O, Freese C (1972) Central crack in plane orthotropic rectangular sheet. Int J Fract Mech 8:49–57